Insights into the Synergistic Roles of Microwave and Fluorination Treatments towards Enhancing the Cycling Stability of P2-Type $Na_{0.67}[Mg_{0.28}Mn_{0.72}]O_2$ Cathode Material for Sodium-Ion Batteries

Funeka P. Nkosi,[a,b] Kumar Raju,[b] Nithyadharseni Palaniyandy,[b] M. V. Reddy,[c,d] Caren Billing,[a] and Kenneth I. Ozoemena[a,*,z]

[a]*Molecular Sciences Institute, School of Chemistry, University of the Witwatersrand, Johannesburg 2050, South Africa*
[b]*Materials Science and Manufacturing, Council for Scientific & Industrial Research (CSIR), Pretoria 0001, South Africa*
[c]*Advanced Batteries Lab, Department of Physics, National University of Singapore, Singapore 117542, Singapore*
[d]*Department of Materials Science and Engineering, National University of Singapore, Singapore 117576, Singapore*

P2-type $Na_{0.67}Mg_{0.28}Mn_{0.72}O_2$ based cathode materials for sodium-ion batteries were prepared using combustion synthesis. The effect of microwave irradiation and fluorination was investigated with the aim to improve the electrochemical performance. Four samples were considered: samples were prepared by the combustion method (NaMgMnO-a) and then either microwave-irradiated or fluorinated (NaMgMnO-ma and NaMgMnO-af, respectively) or both microwave-irradiated and fluorinated (NaMgMnO-maf). The powder XRD analyses showed that pure single phase P2-type powders were successfully prepared. SEM analyses revealed an impact of microwave irradiation and fluorination on the morphology of the materials, suggesting a change in the electrochemical performance. The galvanostatic charge-discharge studies revealed that both microwave irradiation and fluorination improved the capacity and cycle performance. The electrochemical data (from first discharge capacity to coulombic efficiency, capacity retention, cyclability and impedance) show that microwave- and fluorine-treated samples performed better. The key finding clearly shows the impact of microwave irradiation and fluorination processes in suppressing the P2-O2 phase transformation process and the Mn^{3+}-induced Jahn-Teller distortion effect.

Manuscript submitted September 5, 2017; revised manuscript received October 16, 2017. Published November 2, 2017.

The extensive use of lithium-ion batteries (LIBs) in portable electronic devices such as cellphones, laptops, and electric vehicles will eventually increase the cost and the demand of LIBs.[1] Sodium-ion batteries (SIBs) have currently drawn wide attention as the most attractive alternative for LIBs for smart grid applications.[2–4] This is because sodium is cheap and abundant as it is the 4th most abundant element in the earth's crust and is uniformly distributed around the world.[5] SIBs also have high voltage, high energy density and long cycle life.[6–8]

The cathode materials for SIBs include layered oxides, olivines, NASICONs, etc. Among them, layered P2-type manganese oxide (MnO_2)-based materials have been widely studied and continued to attract major research interests as promising cathode materials for SIBs.[9–17] This is due to the abundance of manganese, importantly P2-type MnO_2-based materials offer larger tunnels for the intercalation and de-intercalation of the sodium-ion and have been reported to have high capacities.[18–20] A sodium-ion layered oxide material crystallizes into either P2-type or O3-type structural phases or mixture of both. In the P2-type phase, the sodium-ion is coordinated in the prismatic sites between the TMO_2 (TM = transition metal) sheets and there are two repeating TMO_2 layers in the unit cell (Fig. 1).[2,21,22] In O3-type the sodium-ion is coordinated in the octahedral site and there are three repeating MO_2 layers in the unit cell. P2-type phase is advantageous compared to O3-type phases as it allows easy intercalation and de-intercalation of Na ions and increases the number of the ions that can be intercalated and de-intercalated.[2,23]

Sodium magnesium manganese oxide, $Na_{0.67}Mg_{0.28}Mn_{0.72}O_2$, abbreviated herein simply as NaMgMnO, is well known as high-volumetric capacity/energy cathode material for sodium-ion batteries.[24] It is an important material due to the huge natural abundance of its precursor materials, thus favorable for stationary or grid-scale storage where high energy density and low costs are very critical. But NaMgMnO exhibits capacity fade during electrochemical cycling which would limit its application in grid-scale storage.

This work is aimed at improving the cycle performance of NaMgMnO and, for the first time, the preparation of NaMgMnO cathode material using urea-combustion method is reported. Combustion method of synthesis is regarded an effective and fast method of preparing electrode materials.[26–29] To improve the cycle performance of this material, microwave irradiation and fluorination of this material have been investigated. Our group has shown that microwave irradiation has the ability to improve the morphology and tune the concentration of the Mn^{3+} that causes Jahn-Teller distortion and capacity fade in manganese oxide-based lithium-ion batteries.[30–32] Fluorination, on the other hand, has been found to improve the stability of electrode materials.[33–36] This work interrogates and clearly confirms the synergistic effect of the redox property-enhancing features of microwave irradiation and fluorination toward P2-type NaMgMnO material.

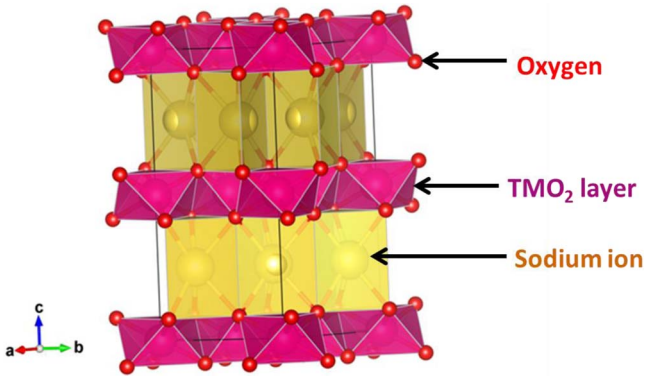

Figure 1. Structural diagram of a typical P2 -type layered material. The diagram was drawn using the VESTA program.[25]

Experimental

Materials.—Sodium carbonate (Na_2CO_3), manganese (II, III) oxide (Mn_3O_4), magnesium oxide (MgO) and urea ($CO(NH_2)_2$) were purchased from Sigma-Aldrich and used without further purification.

*Electrochemical Society Member.
[z]E-mail: kenneth.ozoemena@wits.ac.za

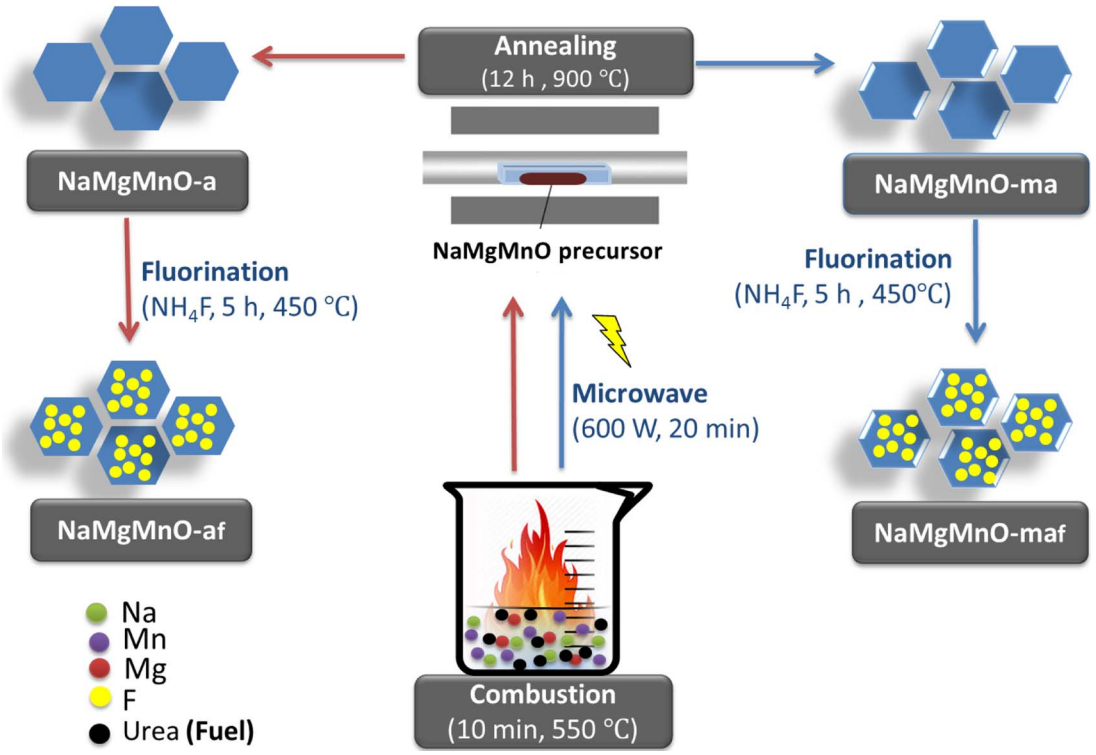

Figure 2. Schematic representation of the general synthesis procedure for the electrode materials.

Synthesis.—Stoichiometric amounts of Na_2CO_3, Mn_3O_4 and MgO were thoroughly mixed using ball milling for 12 h under wet conditions with acetone. The mixture was then properly ground using pestle and mortar and dried in air for 30 min. The resultant mixture was mixed with the appropriate amount of urea, ground and dispersed in de-ionized water, ignited at 500°C in air for ca. 10 min and then left to cool naturally at room temperature. The resultant product was ground into a very fine precursor powder, which was then divided into two batches. One batch was directly annealed at 900°C for 12 h (abbreviated herein as NaMgMnO-a) while the other was first subjected to microwave irradiation (Anton Paar Multiwave 3000 system, λ = 0.12236 m) for 10 min at 600 W before annealing at 900°C for 12 h (product abbreviated herein as NaMgMnO-ma). Portions of each of the NaMgMnO-a and NaMgMnO-ma were fluorinated by calcining the powders with the required amount of NH_4F at 450°C for 5 h, and the resultant products abbreviated herein as NaMgMnO-af and NaMgMnO-maf, respectively. The general scheme for the synthesis is given in Fig. 2.

Characterization.—The prepared powders were analyzed using a PANalytical X'Pert Pro X-ray diffractometer with CuKα radiation (λ = 1.5046 Å) operating at 45 kV and 40 mA. The powder XRD (PXRD) patterns were obtained in a scan range between 5 and 90°. A LEO 1525 field emission scanning electron microscope (FE-SEM) with energy dispersive X-ray (EDX) analysis was used to determine the morphology and confirm the elements present in the materials. An acceleration voltage of 2.00 kV was used and the samples were prepared by putting approximately 0.1 mg of the sample on a carbon tape and coated to prevent charging. The X-ray photoelectron spectroscopy (XPS) using an AXIS ultra DLD spectrometer (KratosAnalytica) and a monochromatic Al *K*α excitation source (1486.6 eV) was used to determine the oxidation states of the elements in the samples. The binding energy (BE) scale was calibrated using a C 1s (BE = 284.6 eV) as the reference.

Electrode fabrication.—The electrochemical performance of the prepared powders was investigated using two-electrode type coin cells. The prepared powders were used as the cathode and sodium chunks were cut into appropriate electrode sizes and used as the anode. The cathode slurry was made by mixing the NaMgMnO powders, carbon black and PVDF binder in a weight ratio of 80:10:10 and ground into a fine powder to mix well. N-methyl-2-pyrrolidone (NMP) solvent was added to the mixture to form a slurry which was stirred overnight at room temperature. The slurry was then coated onto an aluminum foil current collector and dried under vacuum at 110°C for 12 h. The coated aluminum foils were punched and used as the cathode. A 1 M $NaClO_4$ in polycarbonate (PC) served as the electrolyte while a glass microfiber filter paper was used as the separator. Test cells were fabricated in an argon-filled Mbraun glove box. Cyclic voltammetry (CV) studies were carried out on a Bio-Logic Science VMP3-based electrochemistry workstation in a potential range of 1.5 to 4.4 V (vs. Na^+/Na) at a scan rate of 0.1 mV/s. The galvanostatic charge-discharge measurements were carried out using a MACCOR 4000 battery tester. Electrochemical impedance spectroscopy (EIS) measurements were also carried out using the Bio-Logic Science VMP3-based electrochemical workstation over a frequency range from 100 kHz to 1 mHz with an AC signal amplitude of 10 mV. The data acquisition and analysis were done using the EC-Lab V10.32 software.

Results and Discussion

XRD, XPS, SEM and EDX characterization.—Fig. 3 reports the XRD results of the prepared materials NaMgMnO-a, NaMgMnO-ma, NaMgMnO-af and NaMgMnO-maf. The XRD patterns were indexed as a P2-type hexagonal structure with the space group $P6_3/mcm$.[24] The patterns also show an expected diffraction peak at ca. 21 degrees due to the presence of stacking faults of the superlattice layers along the c-axis direction. This is a (1/3, 1/3, 0) peak of superstructure due to the formation of $(\sqrt{3})a$ by $(\sqrt{3})a$ in-plane ordering between (Mg^{2+} and Mn^{3+}) and Mn^{4+}.[24]

The lattice parameters (*a* and *c*), crystal density and cell volume were calculated using Rietveld refinement. For layered materials, lattice parameter *a* represents the interlayer metal-metal distance and lattice parameter *c* represents the inter-slab distance. The

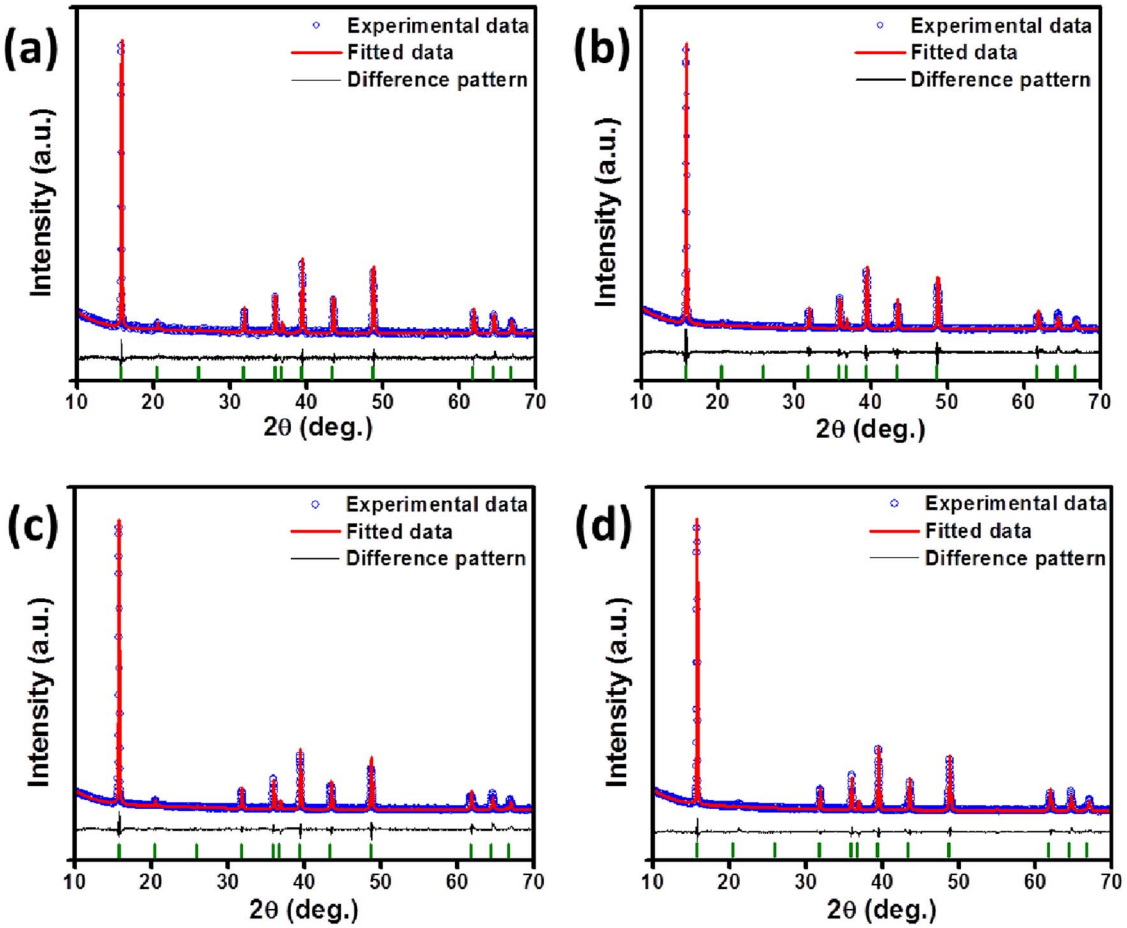

Figure 3. XRD patterns with Rietveld Analysis for (a) NaMgMnO-a, (b) NaMgMnO-af, (c) NaMgMnO-ma and (d) NaMgMnO-maf samples.

crystallographic data summarized in Table I. Within limits of error, the lattice parameters *a* and *c* of the fluorinated and unfluorinated materials are essentially the same. The values of the lattice parameters obtained are comparable to those obtained in literature[37,38] which correspond to $Na_{0.64}Mg_{0.28}Mn_{0.72}O_2$ with $A_1A_1A_1A_1$ cation ordering, i.e the material has the $A_1A_1A_1A_1$ stacking of ordered Mg-Mn layers ($Mg_xMn_{1-x}O_2$ sheets). This ordering of Mg-Mn sheets is confirmed by the presence of the (1/3, 1/3, 0) peak. Importantly, it is clear that the crystal density of the fluorinated materials are higher than those of the unfluorinated complexes, decreasing as follows: NaMgMnO-maf (~84 g cm^{-3}) > NaMgMnO-af (~78 g cm^{-3}) > NaMgMnO-ma (~69 g cm^{-3}) > NaMgMnO-a (~68 g cm^{-3}). The crystal density values suggest that the combination of microwave irradiation with fluorination leads to high molecular packing arrangement of the materials. It confirms that fluorine has been successfully integrated into the structure, resulting in partial replacement of oxygen ions; note that the atomic radius of the fluorine (0.71 nm) is slightly smaller than that of oxygen (0.73 nm). Also, the increased crystal density upon fluorination may be related to fluorine atoms being heavier than oxygen atoms.

Fig. 4 compares the XPS of the deconvoluted peaks of the Mn $2p_{3/2}$ of the four samples, (a) NaMgMnO-a, (b) NaMgMnO-ma, (c) NaMgMnO-af and (d) NaMgMnO-maf. Each of the four X-ray photoelectron spectra yields two binding energy values, with peaks occurring at the expected positions for Mn^{3+} and Mn^{4+} redox states (see Table II). From Table II, it is interesting to observe some unique changes in the percentage concentrations of the Mn^{3+}/Mn^{4+} ratio: upon irradiation with microwave, the ratio decreases by about 25% (compared to that for NaMgMnO-a and NaMgMnO-ma) but dramatically increases when microwave irradiation is followed by fluorination (compare the ratio of 2.24 for NaMgMnO-ma with the ratio of 3.03 for the NaMgMnO-maf). In all cases, however, the Mn^{3+} content is much higher than that of its Mn^{4+} counterpart, resulting in an average valence state of Mn atoms (n_{Mn}) of ca. 3.3+ for each sample (this value would be 3.5+ for a 50:50 ratio of Mn^{3+} and Mn^{4+}). This value is lower than 3.74+ obtained for $Na_{0.53}MnO_2$ by Li et al.[39] which may be related to the substitution of some Mn atoms by Mg in our work. In summary, this result suggests that microwave irradiation and fluorination can increase the amount of the redox-active Mn^{3+}, but without affecting the average valence state of the manganese.

Table I. Summary of refined crystallographic parameters for the prepared NaMgMnO samples.

Material	*a* parameter ± 0.002 (Å)	*b* parameter ± 0.002 (Å)	*c* parameter ± 0.002(Å)	Crystal density ± 0.002 (g cm^{-3})
NaMgMnO-a	5.014	5.014	11.247	67.894
NaMgMnO-ma	5.013	5.013	11.240	68.931
NaMgMnO-af	5.008	5.008	11.274	77.606
NaMgMnO-maf	5.000	5.000	11.224	83.882

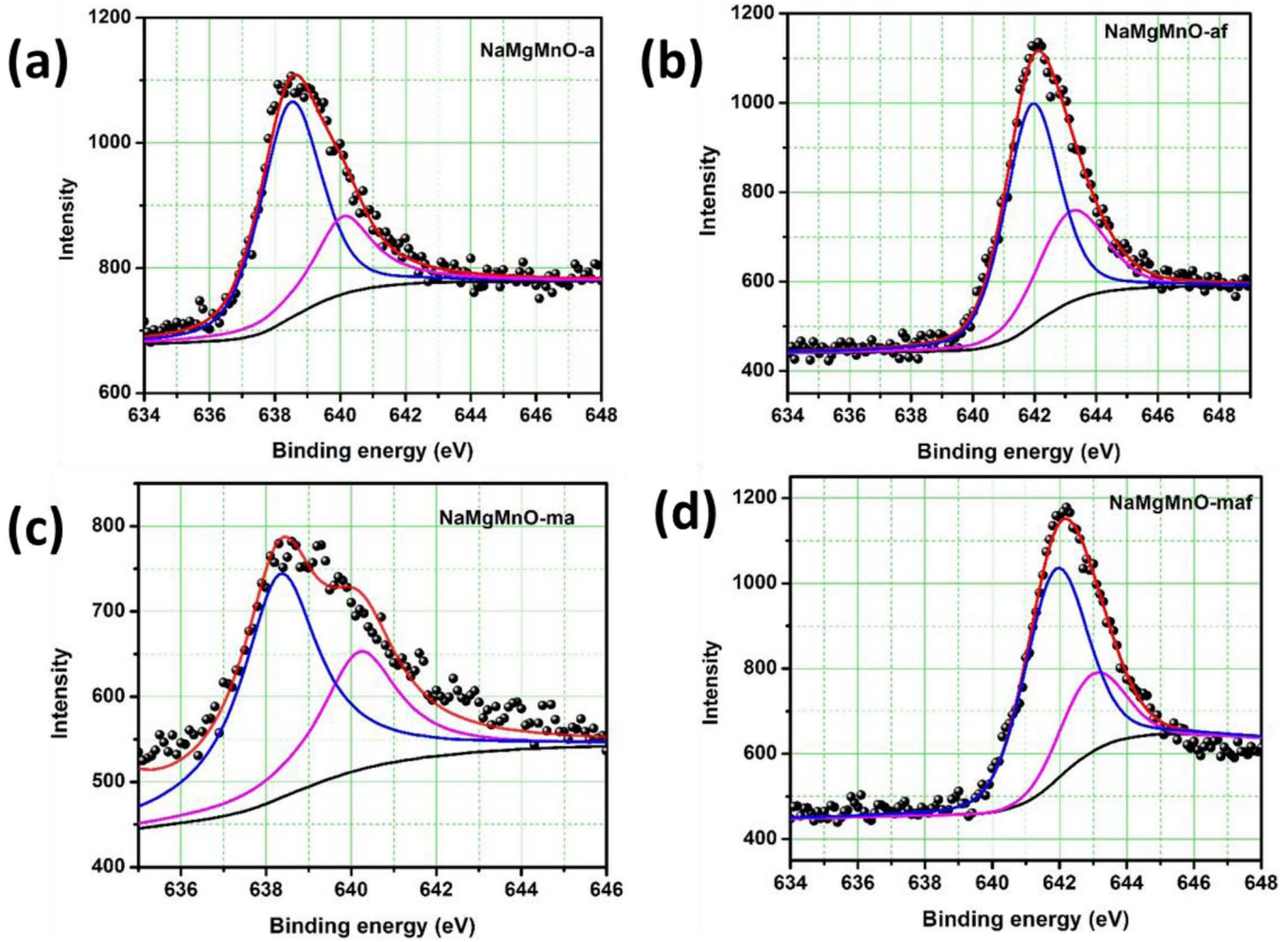

Figure 4. XPS spectra for the (a) NaMgMnO-a, (b) NaMgMnO-ma, (c) NaMgMnO-af and (d) NaMgMnO-maf samples.

The SEM images (Fig. 5) show all the materials as hexagonal plate-like shaped micron-sized particles (1–3 μm diameters). The microwave irradiated material (Figs. 5d, 5e) exhibits clean and smooth surface facets, confirming that they are well-crystallized. Coating of the particles with fluorine leads to surface roughness (Figs. 5g–5k) indicating that the fluorine-doping is generally surface-confined. Surface-doping is expected to improve the electrochemical properties because the transport of Na-ions and electrons during charge and discharge occurs on the surface of the electrodes. Fluorine surface-doping is known to enhance the surface electric conductivity, protect the cathode materials from HF attack, reduce electrolyte oxidation and stabilize the structure of the cathode materials.[40] Figs. 5c, 5f, 5i, 5l also shows the EDX mapping images of the samples confirming the elemental composition of the samples with the fluorine content within the expected 3%. Fig. 6 shows typical EDX mapping of a fluorinated sample (NaMgMnO-af), revealing the expected elements and confirming the presence of fluorine in the sample.

Electrochemical studies.—Fig. 7 compares the cyclic voltammetric evolutions of the four coin cells (made using the synthesized cathode materials) for the fresh cell and after the 100th cycle. The cyclic voltammograms show pairs of ill-defined and broad redox peaks suggesting multi-step reversible reaction processes. Peak broadness is usually indicative of multi-step reaction processes that occur close to one another. Unlike the other materials (Figs. 7b–7d), the pristine material (Fig. 7a) displays redox couples that are broad and nearly indistinguishable indicating that the reactions occur very close to each other in this sample. There are three prominent pairs of redox peaks: (I) at half-wave potential ($E_{1/2}$) of ca. 2.7 V vs. Na/Na$^+$ is ascribed to the Mn^{3+}/Mn^{4+} redox couple, (II) gives broad peaks in

Table II. XPS (Mn-2p$_{3/2}$ spectra) data of the NaMgMnO-a, NaMgMnO-ma, NaMgMnO-af and NaMgMnO-maf samples.

	Binding energy position (eV)		Cation distribution			
Sample	Mn^{4+}	Mn^{3+}	Mn^{4+} (%)	Mn^{3+} (%)	Mn^{3+}/Mn^{4+}	Mn valence (average redox state)
NaMgMnO-a	640.1	638.5	30.9	69.1	2.24	3.31
NaMgMnO-af	643.2	641.9	33.3	66.7	2.00	3.33
NaMgMnO-ma	639.8	638.2	38.8	61.2	1.58	3.39
NaMgMnO-maf	643.0	641.9	24.8	75.2	3.03	3.25

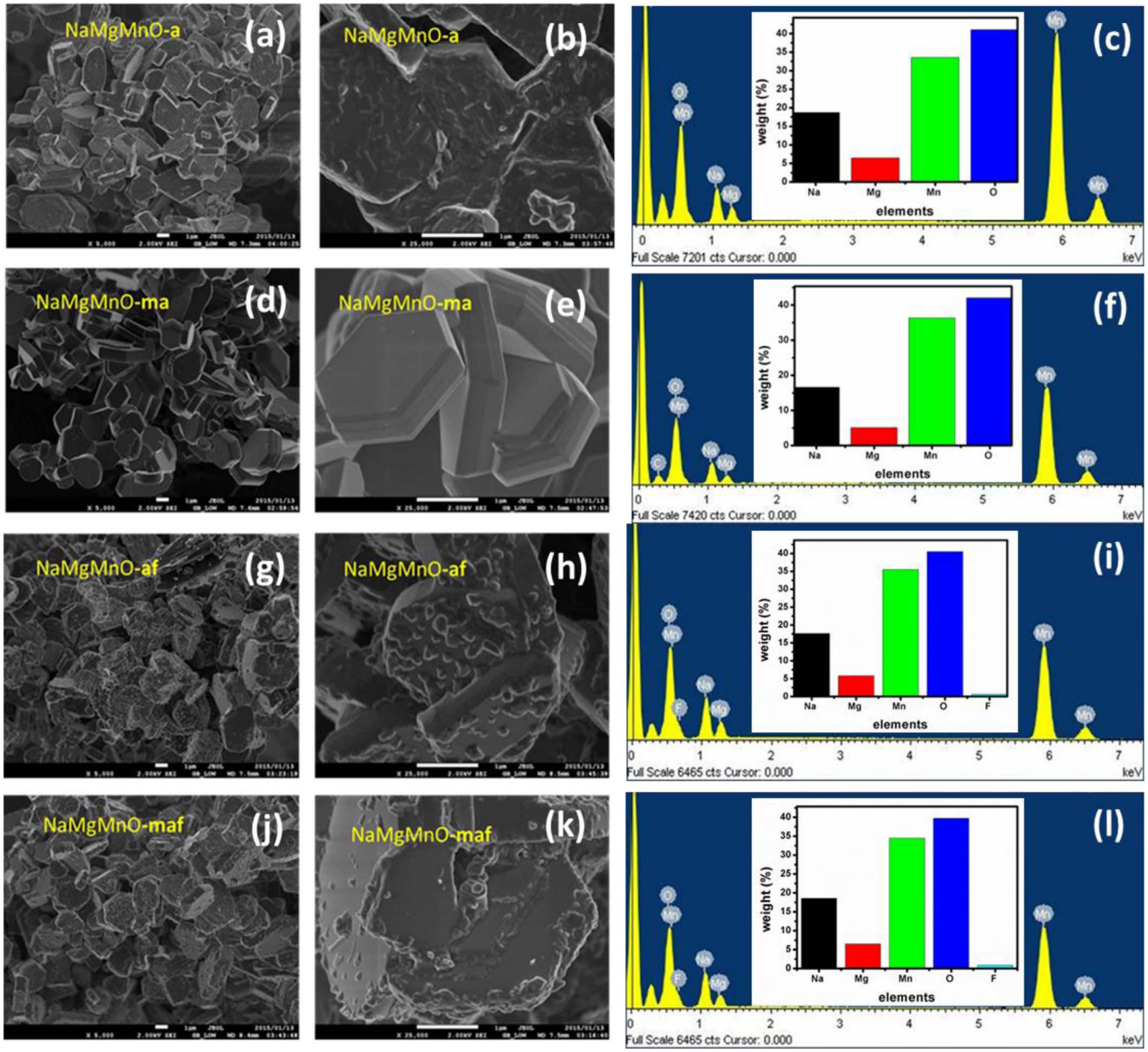

Figure 5. SEM and EDX analysis of NaMgMnO-a (a, b,c), NaMgMnO-ma (d, e,f), NaMgMnO-af (g,h,i) and NaMgMnO-maf (j, k, l) samples.

the $E_{1/2}$ range 3.0–3.3 V vs. Na/Na^+ and is due to the complicated de-sodiation/sodiation processes in the crystal lattice structure, and (III) at ~4.2 V vs. Na/Na^+, observed only in the initial cycle, is due to the P2 – O2 phase transformation and the resultant gliding and expansion of the transition metal layers.[38]

By the 100th cycle, the redox process in the cell with the pristine cathode material as-prepared cell (Fig. 7a) has almost completely disappeared, indicating degradation (poor cycling performance). It is evident that Figs. 7c and 7d are too identical, and yet similar to Fig. 7b at the initial cycle. For the pristine state, both treatments clearly cause a difference in cyclic voltammograms, it seems there is no additional effect if both treatments are used, i.e. one or the other, but not both.

The charge-discharge performances of the materials (1–100 cycles), cycled between 1.5 and 4.4 V at 0.1 C (1C = 260 mA/g) are summarized in Fig. 8. The first charge cycle to 4.4 V corresponds to the extraction (de-sodiation or de-intercalation) of small amounts of sodium ions (low charge capacity). However, upon discharge (sodiation or intercalation) more sodium ions from the sodium source (sodium metal anode) are inserted back into the structure giving rise to higher capacity. The long plateau which appeared around 4.2 V vs Na/Na^+ in the charge curve of all the cells is due to the phase transition from the P2-type to the O2-type structure, with the resultant gliding and expansion of the transition metal layers which leads to irreversible capacity loss, whilst the voltage plateau below 4.0 V is due to the Na^+ and vacancy ordering taking place within the sodium layer. In the O2-type structure, the Na ions sit in the small octahedral sites in the lattice structure while in the P2-type they sit in the large prismatic sites. Therefore, there is a change in the unit cell as the structure changes from a P2-type to O2-type and this induces capacity fade upon cycling. The microwave irradiation and fluorination are observed to increase the capacity of the NaMgMnO material. The discharge capacity for the first cycle is ca. 116, 125, 130 and 140 mAh/g for NaMgMnO-a, NaMgMnO-ma, NaMgMnO-af and NaMgMnO-maf, respectively. The microwave irradiation increased the capacity for both the unfluorinated and fluorinated samples due to the improved

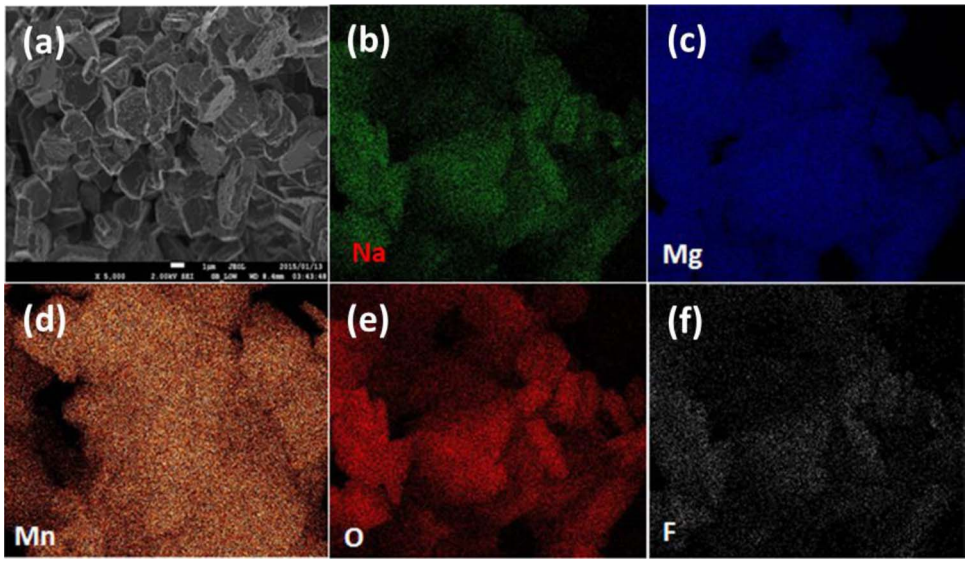

Figure 6. Typical EDX mapping of the samples. These images show the elements present in the NaMgMnO-af sample and confirm the presence of fluorine in the sample.

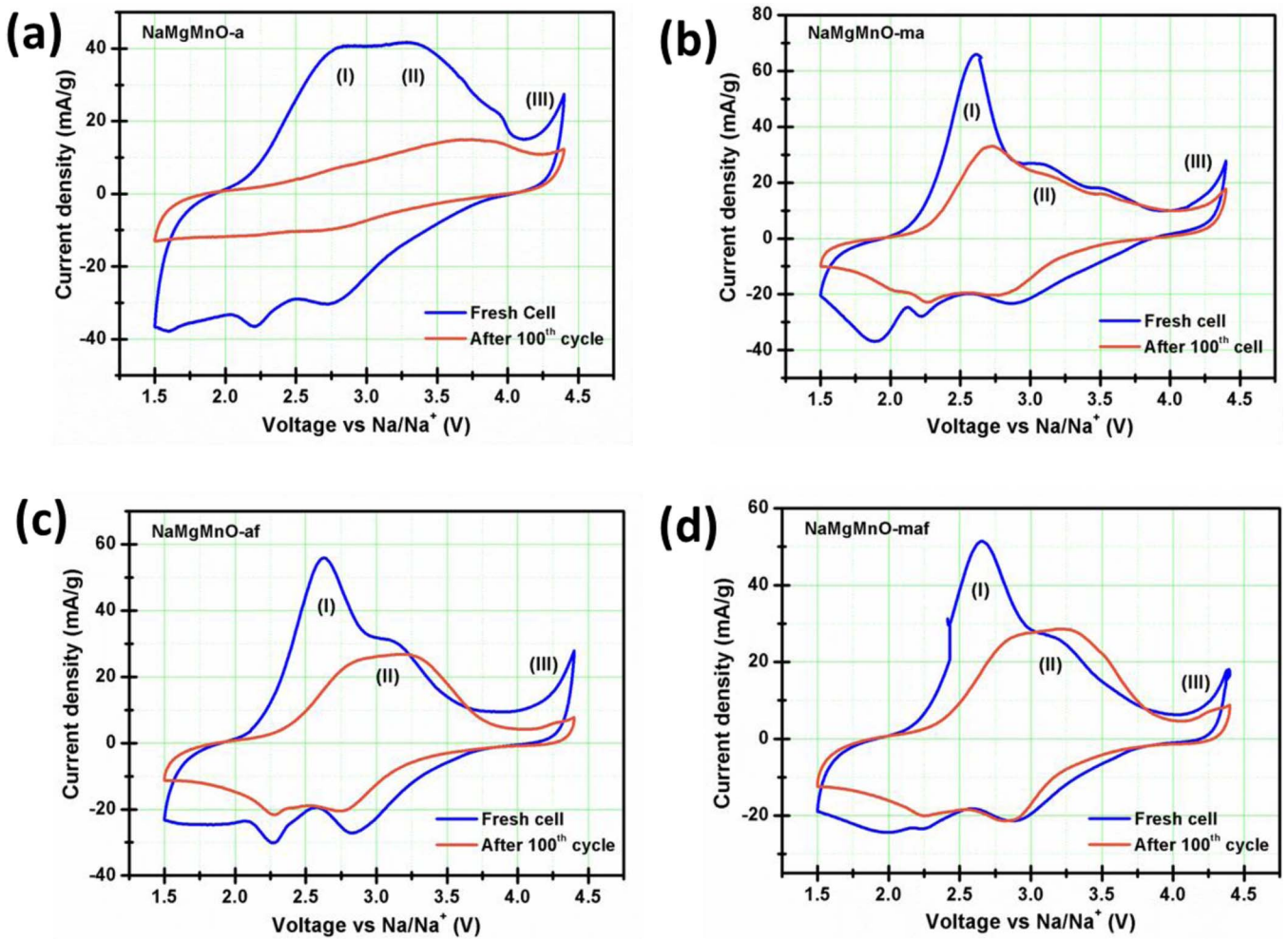

Figure 7. Cyclic voltammograms (current density vs. voltage) of the cells containing the following cathode materials (a) NaMgMnO-a, (b) NaMgMnO-ma, (c) NaMgMnO-af and (d) NaMgMnO-maf. Scan rate: 0.1 mV/s. Voltage range: 1.5–4.4 V vs. Na/Na^+.

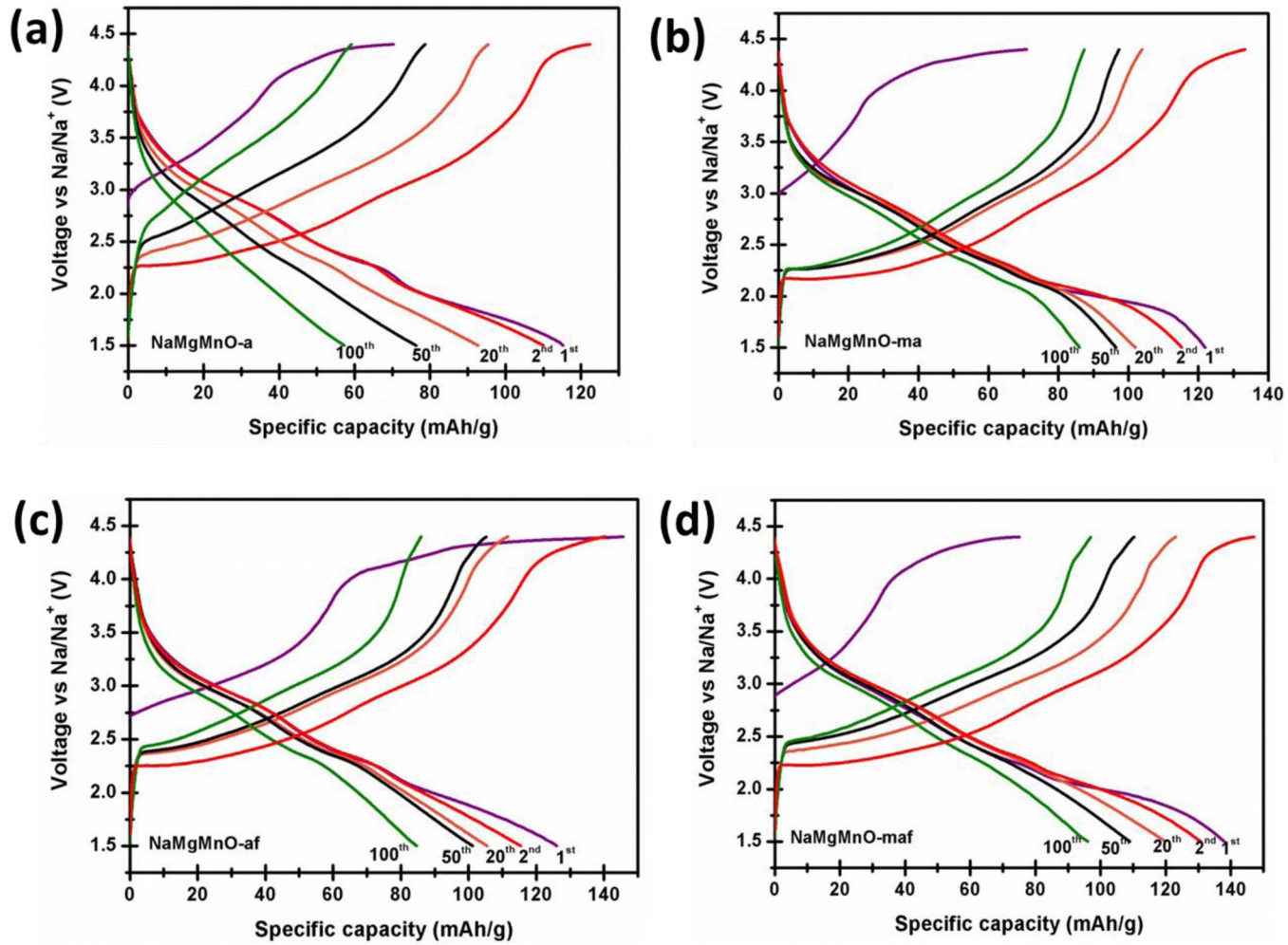

Figure 8. Galvanostatic charge-discharge graphs (voltage vs. specific capacity) of the cells containing the following cathode materials (a) NaMgMnO-a, (b) NaMgMnO-ma, (c) NaMgMnO-af and (d) NaMgMnO-maf.

morphology and crystallinity, as observed in the SEM and XRD analyses. Fluorination increased the capacity because the fluoride-ions are doped on the surface of the NaMgMnO materials and thus result in increased surface electric conductivity and protect the cathode materials from HF attack.

Fig. 9a shows the long-term cycling performance as well as the coulombic efficiency profiles of the NaMgMnO-a, NaMgMnO-ma, NaMgMnO-af and NaMgMnO-maf materials. The capacity retention and coulombic efficiency data are summarized in Table III. All the materials showed similar coulombic efficiency of 100% from about the 5th until the 100th cycle. NaMgMnO-a shows poor capacity retention, only 50% (i.e., 54 mAh/g) of its initial capacity of 108 mAh/g after 100 cycles. At the end of the 100th cycle, NaMgMnO-ma, NaMgMnO-maf and NaMgMnO-af gave capacity retention of 71%, 70% and 62%, respectively. The result clearly shows that microwave and fluorination are able to stabilize the structure of the materials upon continuous cycling. Aside from the phase transformation, the reason for the observed capacity fading may be related to the well-known Jahn-Teller distortion of the high-spin Mn^{3+}.[20–22]

Fig. 9b also shows the rate capability studies of the materials conducted at different current densities (26, 52, 130, 260 and 780 mA/g) with 5 charge-discharge cycles for each step in the voltage range from 1.5 to 4.4 V. The discharge capacity decreased as the current density increased due to the short timescale required for sodiation and desodiation process to occur at the higher current densities. Interestingly, there appears to be no permanent structural or electrode-electrolyte interfacial damage caused by increasing the current density, considering that the final data set returns to a high value as per the initial discharge capacity.

As shown in Table III, there is a discrepancy between the first discharge capacity (DC) and that reported in literature by the groups of Manthiram[8] and Kobama[17] where 220 mAh/g were recorded. While Manthiram group[8] included nickel and cobalt in their material, the work of Kobama and co-workers[17] is similar to the one reported here. Interestingly, however, it is evident from Table III that this present work showed better capacity retention compared to literature.[8,17] The discrepancies may be attributed to the differences in the chemical compositions and synthesis methods adopted. It is common knowledge that synthesis methods and experimental conditions influence the stoichiometry, crystal structure, morphology, and electrochemistry of the electrode materials.

Electrochemical impedance spectroscopy (EIS) was conducted to establish the effects of microwave and fluorination treatments on the kinetics of these NaMgMnO-based electrode materials. The coin cells were analyzed before and after long-hour cycling (i.e. at the end of the 100th cycle) at the open circuit voltage vs. Na/Na^+. The Nyquist plots (Figs. 9c, 9d) were fitted with the electrical equivalent circuit (Fig. 9d, inset) which comprises the expected fitting elements: the solution ohmic resistance of the electrode system (R_e) due to electric conductivity of the electrolyte, separator and electrodes; the surface film resistance (R_{s1}) and capacitance (Q_{s1}), referring to the resistance and capacitance (as a constant-phase element) due to

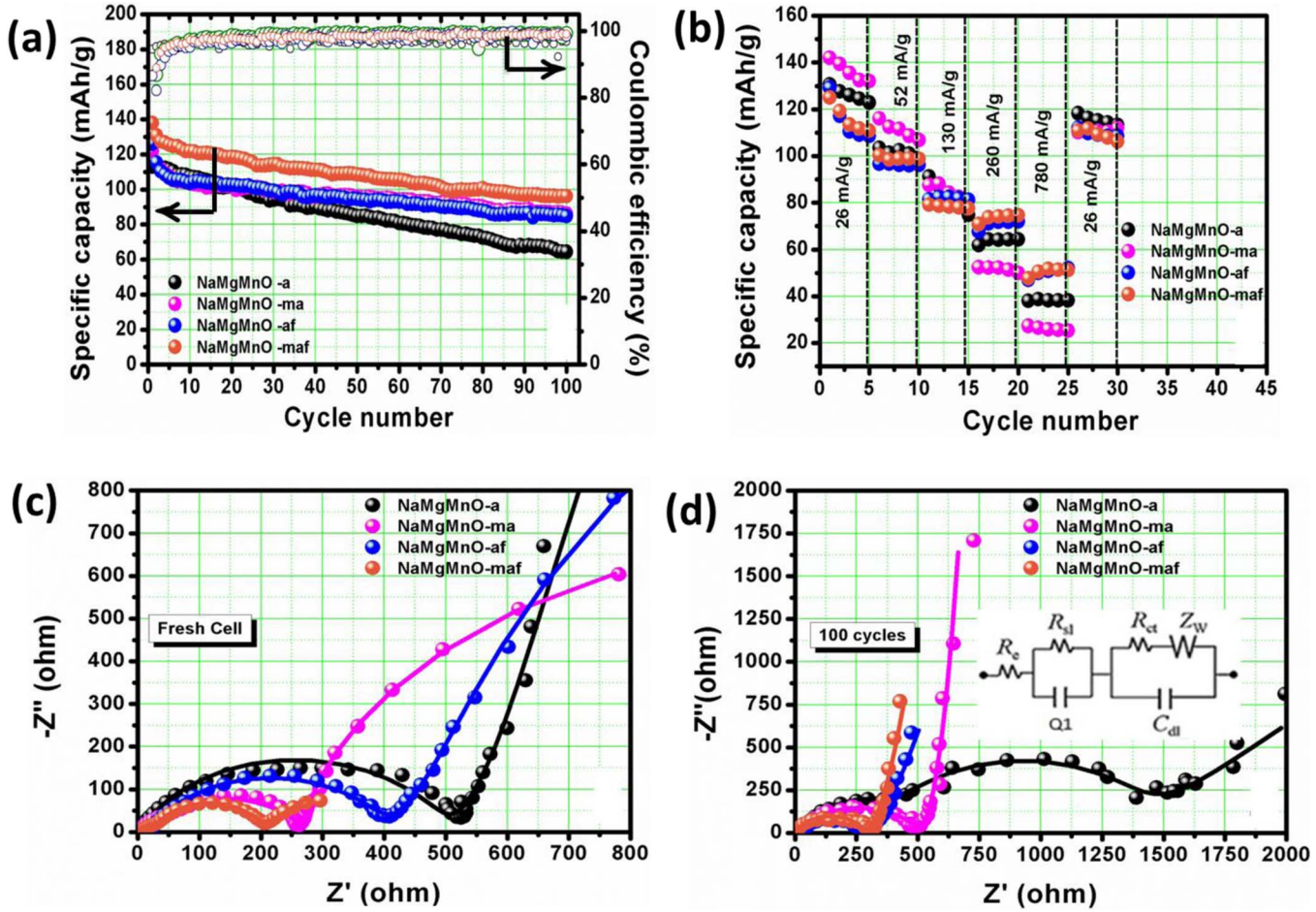

Figure 9. (a) Discharge capacity vs cycle number and coulombic efficiency graphs of the cells containing the NaMgMnO materials, (b) rate performance at different current densities and (c,d) Nyquist plots (Z″ vs. Z′) measured before (OCV) and after cycling (100 cycles). The dots and the straight line represent the experimental and fitted data, respectively. Inset (d) is the electrical equivalent circuit used in the fitting of the experimental data.

Table III. Summary of discharge capacity and capacity retention of NaMgMnO samples.

Material	DC at the 1st cycle (mAh/g)	CE at the 1st cycle (%)	CR at the 20th cycle (%)	CR at the 30th cycle (%)	CR at the 50th cycle (%)	CR at the 100th cycle (%)
NaMgMnO-a	108	66	81	76	67	50
NaMgMnO-ma	123	57	82	82	78	71
NaMgMnO-af	128	113	81	79	75	62
NaMgMnO-maf	140	53	86	83	79	70
Ref. 8	220	68	80	68	n/a	n/a
Ref. 17	220	~96	~80	~68	n/a	n/a

Key: DC = Discharge capacity; CE = Coulombic efficiency; CR = Capacity retention; n/a = Not available.

Table IV. Impedimetric data of the various NaMgMnO-based cathode materials obtained by fitting the Nyquist plots acquired prior to and after the 100th cycle using the equivalent circuit (Fig. 9d, inset).

Material	Aging cells	R_e (±5Ω)	R_{s1} (±5Ω)	$R_{(ct)}$(±5Ω)	W_s (±10Ω)
NaMgMnO-a	Fresh cells	3.50	21.79	516.40	39.50
	100th cycle	36.30	3.09	1840.00	182.40
NaMgMnO-ma	Fresh cells	3.50	2.18	261.90	1.30
	100th cycle	6.20	13.14	494.80	23.40
NaMgMnO-af	Fresh cells	19.40	3.83	386.30	37.20
	100th cycle	23.80	41.18	256.80	45.20
NaMgMnO-maf	Fresh cells	6.20	25.00	166.70	65.70
	100th cycle	4.10	31.62	281.60	27.70

the electrode-electrolyte interface layer formed on the electrode surface; the charge-transfer resistance (R_{ct}) and interfacial capacitance (C_{dl}), corresponding to the sodium intercalation/de-intercalation process arising at the electrode-electrolyte interface; and the Warburg element (Z_w) describing the solid-state diffusion of sodium-ions through the lattice structure of the compound, signified by the straight sloping line (~45°) at the low frequency region. The values obtained from the fitted EIS data are summarized in Table IV. With the exception of the NaMgMnO-af, the charge transfer resistance of the other three compounds obtained after the 100th cycle are larger compared to the initial cycling, which suggests that NaMgMnO-af cell experienced slight activation, hence its enhanced conductivity and kinetics of the Na^+ ions during the repetitive cycling. From the total series resistance ($R_e + R_{s1} + R_{ct}$), the percentage increase of resistance after the 100th cycle are the NaMgMnO-af (−21%) < NaMgMnO-maf (60%) NaMgMnO-ma (92%) < NaMgMnO-a (247%), clearly showing that the best-conducting materials are the fluorinated materials while the pristine complex is the bad-performer.

The Na-ion diffusion coefficients were obtained after 100 cycles using EIS data as described in the literature[41,42] and were found to be 9.3×10^{-14}, 2.6×10^{-12}, 1.2×10^{-12} and 4.3×10^{-12} $cm^2\ s^{-1}$ for NaMgMnO-a, NaMgMnO-ma, NaMgMnO-af and NaMgMnO-maf, respectively. The microwaved and fluorinated complexes gave the highest values compared to the pristine sample. The differences in the values may be due to the morphological differences of the samples. The clean and smooth surface facets due to microwave irradiation observed in NaMgMnO-ma improves the contact of the sample with the electrolyte and the transport of Na-ions and electrons during charge and discharge. The surface doping with fluoride-ions in NaMgMnO-af and NaMgMnO-maf stabilizes the structure and reduces the manganese dissolution reaction and the electrolyte oxidation.

Conclusions

The urea-based combustion method has been utilized to synthesize P2-type $Na_{0.67}Mg_{0.28}Mn_{0.72}O_2$ sodium-ion battery cathode materials with well-defined Mg-Mn cation ordering. Surface fluorination contributed to improving the electrochemical performance of the materials such as discharge capacity, cycling efficiency and cycling stability. Microwave irradiation for the un-fluorinated sample enhanced the morphology and crystallinity which, in turn, improved the capacity and capacity retention of the sample. But microwave irradiation combined with fluorination resulted in even better electrochemical performance, proving the synergy of these dual treatment methods to curb the negative P2-O2 phase transformation process and the Mn^{3+}-induced Jahn-Teller effect.

Acknowledgment

FPN thanks the CSIR for the doctoral studentship and the National University of Singapore for a research visit to validate some of the characterization processes.

References

1. M. Reddy, G. Subba Rao, and B. Chowdari, *Chemical reviews*, **113**, 5364 (2013).
2. N. Yabuuchi, K. Kubota, M. Dahbi, and S. Komaba, *Chemical reviews*, **114**, 11636 (2014).
3. M. D. Slater, D. Kim, E. Lee, and C. S. Johnson, *Advanced Functional Materials*, **23**, 947 (2013).
4. B. L. Ellis and L. F. Nazar, *Current Opinion in Solid State and Materials Science*, **16**, 168 (2012).
5. D. Kim, E. Lee, M. Slater, W. Lu, S. Rood, and C. S. Johnson, *Electrochemistry Communications*, **18**, 66 (2012).
6. V. Palomares, P. Serras, I. Villaluenga, K. B. Hueso, J. Carretero-González, and T. Rojo, *Energy & Environmental Science*, **5**, 5884 (2012).
7. H. Pan, Y. Hu, and L. Chen, *Energy & Environmental Science*, **6**, 2338 (2013).
8. M. D. Slater, D. Kim, E. Lee, and C. S. Johnson, *Advanced Functional Materials*, **23**, 947 (2013).
9. R. Shanmugam and W. Lai, *Journal of the Electrochemical Society*, **162**, A8 (2015).
10. K. Kubota and S. Komaba, *Journal of the Electrochemical Society*, **162**, A2538 (2015).
11. R. J. Clément, P. G. Bruce, and C. P. Grey, *Journal of the Electrochemical Society*, **162**, A2589 (2015).
12. J. Zheng, P. Yan, W. H. Kan, C. Wang, and A. Manthiram, *Journal of the Electrochemical Society*, **163**, A584 (2016).
13. J. Kim and G. Amatucci, *Journal of the Electrochemical Society*, **163**, A696 (2016).
14. G. Venkatesh, B. Kishore, R. Viswanatha, D. Aurbach, and N. Munichandraiah, *Journal of the Electrochemical Society*, **164**, A2176 (2017).
15. N. Nguyen, K. Kim, K. H. Choi, H. Jeon, K. Lee, M. Ryou et al., *Journal of the Electrochemical Society*, **164**, A6308 (2017).
16. C. Ma, J. Alvarado, J. Xu, R. J. Clément, M. Kodur, W. Tong et al., *Journal of the American Chemical Society*, **139**, 4835 (2017).
17. W. Pang, X. Zhang, J. Guo, J. Li, X. Yan, B. Hou et al., *Journal of Power Sources*, **356**, 80 (2017).
18. H. Wang, B. Yang, X. Liao, J. Xu, D. Yang, Y. He et al., *Electrochimica Acta*, **113**, 200 (2013).
19. N. Yabuuchi, M. Kajiyama, J. Iwatate, H. Nishikawa, S. Hitomi, R. Okuyama et al., *Nature materials*, **11**, 512 (2012).
20. S. Kim, D. Seo, X. Ma, G. Ceder, and K. Kang, *Advanced Energy Materials*, **2**, 710 (2012).
21. R. Berthelot, D. Carlier, and C. Delmas, *Nature materials*, **10**, 74 (2011).
22. M. Guignard, C. Didier, J. Darriet, P. Bordet, E. Elkaïm, and C. Delmas, *Nature materials*, **12**, 74 (2013).
23. X. Wu, J. Guo, D. Wang, G. Zhong, M. J. McDonald, and Y. Yang, *Journal of Power Sources*, **281**, 18 (2015).
24. N. Yabuuchi, R. Hara, K. Kubota, J. Paulsen, S. Kumakura, and S. Komaba, *Journal of Materials Chemistry A*, **2**, 16851 (2014).
25. K. Momma and F. Izumi, *Journal of Applied Crystallography*, **44**, 1272 (2011).
26. S. Chitra, P. Kalyani, T. Mohan, R. Gangadharan, B. Yebka, S. Castro-Garcia et al., *Journal of electroceramics*, **3**, 433 (1999).
27. W. Yang, G. Zhang, J. Xie, L. Yang, and Q. Liu, *Journal of Power Sources*, **81**, 412 (1999).
28. K. Lee, H. Choi, and J. Lee, *Journal of Materials Science Letters*, **20**, 1309 (2001).
29. M. V. Reddy, B. L. Wei Wen, K. P. Loh, and B. V. R. Chowdari, *ACS applied materials & interfaces*, **5**, 7777 (2013).
30. C. J. Jafta, K. Raju, M. K. Mathe, N. Manyala, and K. I. Ozoemena, *Journal of the Electrochemical Society*, **162**, A768 (2015).
31. F. P. Nkosi, C. J. Jafta, M. Kebede, L. le Roux, M. K. Mathe, and K. I. Ozoemena, *RSC Advances*, **5**, 32256 (2015).
32. K. Raju, F. P. Nkosi, E. Viswanathan, M. K. Mathe, K. Damodaran, and K. I. Ozoemena, *Physical Chemistry Chemical Physics*, **18**, 13074 (2016).
33. R. Tripathi, S. M. Wood, M. S. Islam, and L. F. Nazar, *Energy & Environmental Science*, **6**, 2257 (2013).
34. S. Kang and K. Amine, *Journal of Power Sources*, **146**, 654 (2005).
35. P. Barpanda, J. Chotard, N. Recham, C. Delacourt, M. Ati, L. DuPont et al., *Inorganic chemistry*, **49**, 7401 (2010).
36. P. Yue, Z. Wang, H. Guo, X. Xiong, and X. Li, *Electrochimica Acta*, **92**, 1 (2013).
37. J. Paulsen, R. Donaberger, and J. Dahn, *Chemistry of materials*, **12**, 2257 (2000).
38. H. Hou, B. Gan, Y. Gong, N. Chen, and C. Sun, *Inorganic chemistry*, **55**, 9033 (2016).
39. J. Li, H. Lü, X. Zhang, Y. Xing, G. Wang, H. Guan et al., *Chemical Engineering Journal*, **316**, 499 (2017).
40. G. G. Amatucci and N. Pereira, *Journal of Fluorine Chemistry*, **128**, 243 (2007).
41. C. J. Jafta, K. I. Ozoemena, M. K. Mathe, and W. D. Roos, *Electrochimica Acta*, **85**, 411 (2012).
42. M. A. Kebede, S. Yannopoulos, L. Sygellou, and K. I. Ozoemena, *Journal of the Electrochemical Society*, 2017 (accepted).